



Flow structure of unconfined turbidity currents interacting with an obstacle

Richard I. Wilson¹ · Heide Friedrich² · Craig Stevens^{3,4}

Received: 4 September 2017 / Accepted: 19 September 2018
© Springer Nature B.V. 2018

Abstract

Driven by a growing importance to engineered structures, investigating the flow characteristics of turbidity currents interacting with a basal obstruction has become popular over the last three decades. However, research has focused on confined studies or numerical simulations, whereas in situ turbidity currents are typically unconfined. The present study investigates experimentally the velocity and turbulence structure of an unconfined turbidity current, in the immediate regions surrounding a rectangular obstacle. Initial density of the current, and substrate condition is varied. Through a novel technique of installing ultrasonic probes within the obstacle, the presence of a velocity recirculation region immediately upstream and downstream of the obstacle is revealed and confirmed with high-resolution imagery. This was found to be comparable to previous confined studies, suggesting that stream-wise velocity profile structure is somewhat independent of confinement. The obstacle was found to reduce velocity and turbulence intensity maxima downstream of the obstacle when compared with unobstructed tests.

Keywords Unconfinement · Obstacle · Turbidity current · Turbulence · Mixing

✉ Richard I. Wilson
rwilson@tonkintaylor.co.nz

Heide Friedrich
h.friedrich@auckland.ac.nz

Craig Stevens
craig.stevens@niwa.co.nz

¹ Water Engineering, Tonkin & Taylor Ltd, Auckland, New Zealand

² Department of Civil and Environmental Engineering, University of Auckland, Auckland, New Zealand

³ National Institute of Water and Atmospheric Research, Wellington, New Zealand

⁴ Department of Physics, University of Auckland, Auckland, New Zealand

1 Introduction

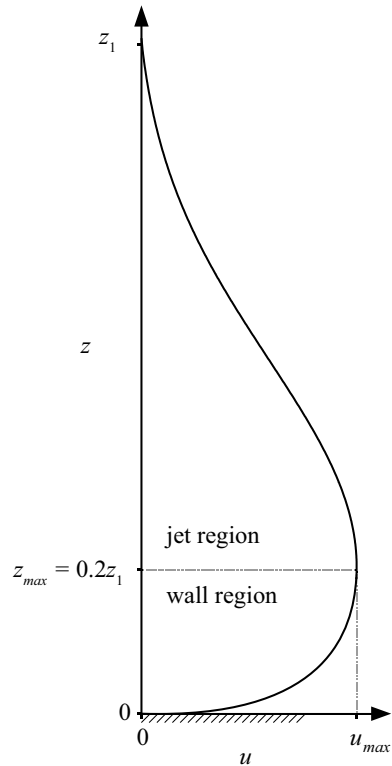
Turbidity currents are sediment-laden flows, which occur in both saltwater and freshwater environments. They are a form of density current, which is caused by a dense fluid interacting with a generally, less-dense ambient fluid. Buoyancy forces act upon the density difference, causing a propagating current. In the case of turbidity currents, entrained sediment is commonly the cause of the density difference between the two fluids, however, differences in temperature and salinity can also be a contributing factor. Turbidity currents are initiated by a range of different processes, which Meiburg and Kneller [1] review in detail. This typically includes rivers in flood reaching river mouths or reservoirs, where the rapid decrease in flow velocity causes the entrained sediment plume to settle and subsequently form a propagating current (hyperpycnal flow). Alternatively, currents may be initiated by submarine slope failures or anthropogenic processes, such as the deposition of dredged sediment at the heads of submarine canyons [2].

In recent years, there has been a growing interest in understanding the dynamics of turbidity currents as they interact with obstacles. This has been driven by a number of practical reasons. Firstly, turbidity currents have been recognized as being the cause of submarine cable rupture in numerous events [3–8]. They also pose a risk to oil and gas pipelines [9]. Secondly, there has been interest in how turbidity currents interact with aquatic flora. Through experimental studies, Testik and Yilmaz [10] showed that in the presence of vegetation, gravity currents transition to a propagation phase dominated by resistive drag forces. Likewise, Ho and Lin [11] showed that head development reduced in gravity currents travelling through emergent vegetation, with increasing vegetation density. Lastly, turbidity currents contribute to the sedimentation of reservoirs, which is a significant threat to their sustainability if not adequately managed [12]. Globally, the annual loss of reservoir storage capacity to sedimentation is greater than that gained from construction of new reservoirs [13]. Among other methods, the use of rigid obstacles as a barrier to turbidity current propagation has since been investigated as a mitigative option by impeding sediment transport [13–15].

In the latter case, research on obstacles has focused on their ability to halt current propagation. Through laboratory experiments and numerical simulations, Oehy and Schleiss [14] investigated the effects of a solid Gaussian-shaped obstacle and permeable screen on confined turbidity currents. They analyzed velocity distributions surrounding the obstructions using an ultrasonic Doppler velocity profiler (UVP), showing that both obstructions are effective in reducing current velocity. They also showed that downstream obstacle deposits were reduced by a factor of 6–8, compared to unobstructed flow. More recently, Yaghoubi et al. [15] studied the effect inlet concentration had on turbidity current behaviour over two consecutive triangular obstacles. They showed that a high concentration, low velocity region develops upstream of each obstacle, and that deposition is greater prior to the upstream obstacle. Confined turbidity current–obstacle interaction has also been extensively studied through computational models [14, 16–21].

Turbidity currents have a distinct vertical velocity profile, which Altinakar et al. [22] showed through experiments are similar to a wall jet with an upper and lower region. Turbulence in the lower wall region is dictated by bottom shear, whilst shearing at the boundary of the ambient fluid causes turbulence in the upper jet region. Kneller et al. [23] showed the velocity profile can be represented by a log-Gaussian curve, where the maximum forward velocity occurs at a height of $z_{max} \approx 0.2z_1$, where z_{max} is the maximum current height (Fig. 1). Other unobstructed studies have shown maximum velocity to occur at

Fig. 1 Typical vertical profile of stream-wise turbidity current velocity distribution. The log-Gaussian profile includes a maximum velocity (u_{max}), which occurs as a height of $z_{max}=0.2z_1$. Surrounding the height of u_{max} is a lower wall region and an upper jet region



$z/z_{max} \approx 0.2-0.3$ [14, 22, 24, 25]. Eggenhuisen and McCaffrey [26], who argued that vertical velocity turbulence is the most important velocity field component to a turbidity current's sediment transport capacity, studied velocity and turbulence intensity profiles of turbidity currents propagating over a rough, basal obstruction. Both obstructed and unobstructed tests showed a local intensity maximum both above and below the velocity maximum—in the regions where velocity experiences the greatest spatial change. The lower maximum, however, was 41–81% greater for the obstructed case. Interestingly, they found this lower maximum to dissipate upwards downstream, and suggested that due to dispersion-diffusion theory, single roughness elements may counteract density stratification and increase turbidity current runout distances.

Through experiments on triangular obstacles under quasi-steady conditions, Oshaghi et al. [25] found turbidity currents exhibited a reduction in maximum velocity and current inertia with increasing obstacle height. Yaghoubi et al. [15] showed through acoustic Doppler velocimeter (ADV) profile measurements that immediately downstream of the first obstacle, a small recirculation region was present at the bed interface. They also showed a larger recirculation region, approximately equal height to the obstacle (150 mm), to occur between the two obstacles, which was attributed to an adverse pressure gradient.

In recent years, considerable work has gone into developing 2D and 3D numerical models of confined turbidity currents interacting with obstacles [16, 19–21, 27]. Models have also been produced for unconfined turbidity currents [28–30]. It is common practice to validate numerical models with experimental studies, which is generally achieved through comparison

of non-dimensional, spatio-temporal current evolution and flow parameters such as Reynolds and Froude numbers. Given the lack of quantitative experimental studies of unconfined turbidity currents interacting with obstacles, there is a need to investigate how the velocity structure of a turbidity current develops over an obstruction, to provide a basis for future numerical model validation.

Understanding the role substrate roughness plays on experimental turbidity currents is important, especially when considering the suitability of experimental studies as scaled substitutes for field turbidity currents. Numerous experimental studies have considered the effects of basal roughness, from employing sediments in the range of 0.2–25 mm diameter [29, 31, 32], to the use of arrayed cylinders of height 10–50 mm [33, 34]. Typically, substrate roughness has been shown to reduce current propagation velocities due to increased shear stress at the basal interface, and also entrainment of ambient fluid resting within the roughness layer, as suggested by [33].

To date, experimental and numerical turbidity currents have tended to be modelled in a quasi-two-dimensional unconfined environment. Therefore, there have been few unconfined studies incorporating obstacles [35, 36], less so for studies which quantify velocity structure within the current itself. Natural turbidity currents occurring in lakes, reservoirs and submarine fans are laterally unconfined. Therefore, lateral movements are important to consider in experimental models, as they can reduce the rate at which currents spread longitudinally [37]. Therefore, there is a need to better quantify the velocity structure of the passing head and body in immediate regions surrounding an obstacle in unconfined conditions. This provides insight into how the obstacle changes turbidity current flow behaviour and enables the implications of unconfinement to be investigated through lateral observations. It is also of interest to understand the role in which substrate roughness plays on these changes in turbidity current flow behaviour.

In the following study, we integrate the photometric techniques of Wilson et al. [38] with UVP analysis, by introducing a novel method of placing UVP probes within an obstacle. This enables detailed velocity information near the obstacle and bed surface to be measured. The key objectives are to: (i) investigate velocity and turbulence profiles of unconfined, lock-exchange turbidity currents traversing a rectangular obstacle, identifying key regions, (ii) compare the characteristics of turbulent regions with confined studies, and determine how they are affected by varying substrate and initial density and (iii) to discuss the effect of unconfinement on stream-wise current behaviour, how it compares with confined studies and the impairing effect of the obstacle on flow velocity and turbulence.

A finite-release, lock-exchange experimental setup was chosen due to its popularity and suitability for photometric analysis [30, 39–41]. It also represents finite-release events, such as the collapsing of sedimentary shelves in submarine canyons. Experiments were completed in an unconfined basin, where turbidity currents interacting with a rectangular obstacle were examined under four obstacle and substrate conditions: no-obstacle/smooth substrate, no-obstacle/rough substrate, obstacle/smooth substrate and obstacle/rough substrate. Turbidity currents of varying density, velocity and turbulence profiles were measured in regions of interest, and their relation to lateral movements and entrainment mechanisms are discussed.

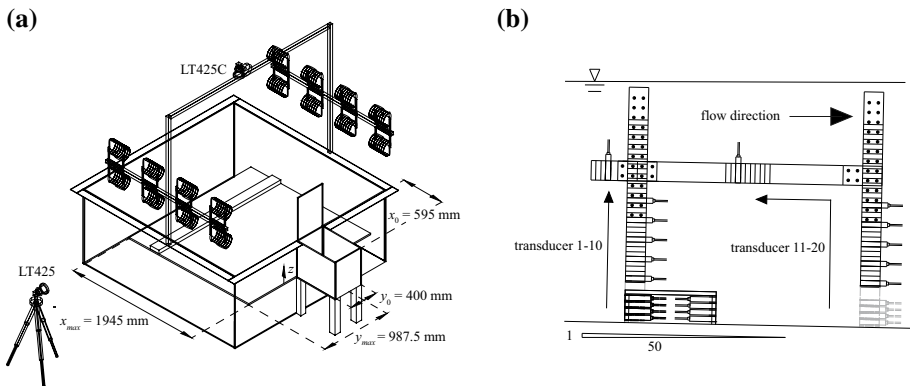
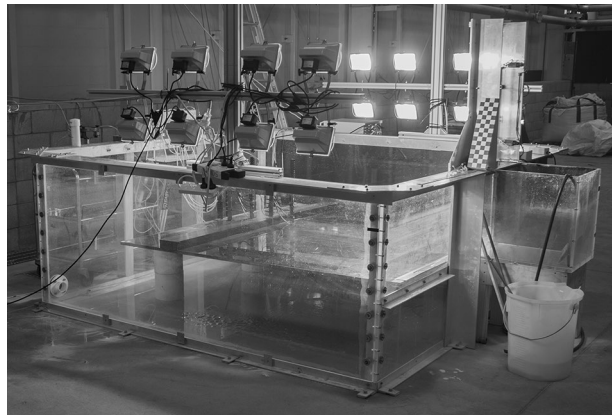


Fig. 2 **a** Schematic of the unconfined lock-exchange basin, outlining key dimensions and the location of cameras and halogen lamps. **b** Configuration of the UVP transducers within the obstacle and instrument rack. The upstream transducers were labelled 1–10 upwards, downstream transducers were similarly labelled 11–20. For tests with no obstacle, the vertical racks were replaced with longer equivalents (shown in grey) to ensure profiles were taken in the same location as obstacle tests

Fig. 3 Perspective view of the experimental basin, highlighting the illumination arrangement, false glass floor and lock-exchange box and gate



2 Experimental setup and methodology

Lock-exchange released turbidity currents were physically modelled in an unconfined basin, within the Hydraulic Engineering Laboratory at the University of Auckland. The 2445 mm long, 2415 mm wide and 1040 mm high basin included a false glass floor set at a 2% downward slope, measuring $x_{max} = 1945$ mm long by $2y_{max} = 1975$ mm wide (Fig. 2a). A lock-box and gate-release mechanism, sealed with petroleum jelly was located in the centre of the upstream wall. The lockbox measured $x_0 = 595$ mm long by 400 mm wide and the gate was operated mechanically by a remote control (Fig. 3). For all tests, the basin was filled with tap water to a height of $z_0 = 300$ mm, measured at the lockbox gate. A 140 mm long, 50 mm high rectangular obstacle which spanned the width of the glass floor was installed at $x/x_0 = 2.45$. For half of the tests, a rough substrate of comparable roughness to La Rocca et al. [29] was installed near the obstacle on

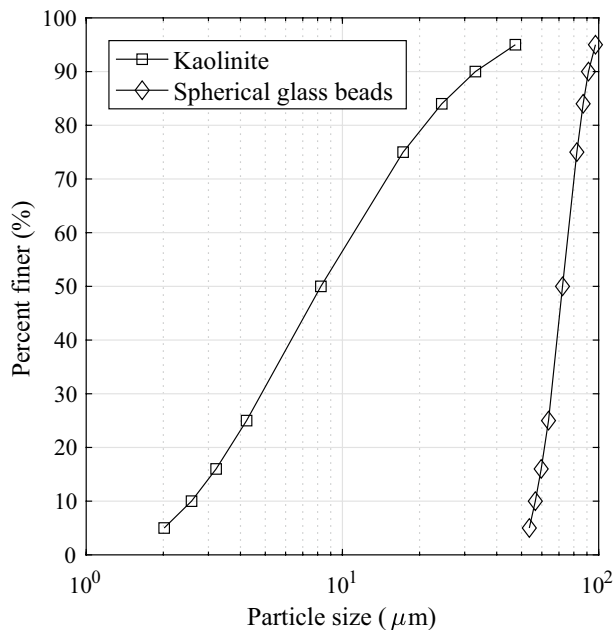
the top of the glass floor. The substrate, which consisted of $D_{50}=0.85$ mm sand glued to a 1.6 mm thick steel sheet, had equal dimensions to the glass floor.

The generated turbidity currents were composed with a 1:1 ratio by mass of spherical glass beads and kaolinite clay. Prior to each test, the sediment was mechanically mixed for a minimum of 30 s in a bucket with 6 L of water. The temperature of the ambient fluid was measured to optimize the sediment required and calculate kinematic viscosity, ν . The sediment mass was varied to create four different initial theoretical densities: $\rho_0=1020$, 1040, 1060 and 1080 kg m⁻³. The grain size distribution of both sediments is shown in Fig. 4. To the authors' knowledge, there have not been any studies to date that have sought to clearly define the density at which a clay-based turbidity current starts to experience non-Newtonian characteristics. The study of Jacobson and Testik [42] investigated non-Newtonian turbidity currents with densities of 1020–1200 kg m⁻³. This overlaps with the present study's range, therefore, non-Newtonian behavior cannot be ruled out at the higher densities within our study. However, we did not experience any significant change in behavior to suggest that a change in Newtonian state occurred.

The lockbox incorporated a displacement bucket, of equal volume to the sediment slurry. Prior to gate opening, the displacement bucket was removed and the slurry poured in, ensuring the free surface level of the basin and lockbox were equal. This reduced the formation of standing waves on the free surface.

To analyze velocity, u , and turbulence intensity, I , profiles of the turbidity currents, a Met-Flow UVP-DUO was used with 20 ultrasonic transducers. Ultrasonic Doppler velocity profiling (UVP) is a velocity measuring technique in which submerged, 8 mm diameter cylindrical transducers send a 4 MHz a burst of ultrasonic signals into a receiving fluid body. The pulsed signals travel to numerous virtual channels, which in the present study amounted to 128. The signals are reflected by moving particles within the fluid and the resultant frequency of the signal is recorded by the transducer. Using Doppler theory, the

Fig. 4 Grainsize distribution of the kaolinite clay and spherical glass bead compounds used for the experimental turbidity currents. Measurements were made using a Malvern Mastersizer 2000



velocity in the axial direction of the transducer can be measured. Combining all velocity measurements allows a one-dimensional velocity profile to be obtained for each transducer. A series of initial tests were conducted to optimize the UVP-DUO settings and maximize the signal-to-noise (SNR) ratio. These settings are listed in Table 1.

A centred, vertical array of nine transducers facing the lockbox was located at both the upstream obstacle face ($x/x_0=2.45$) and downstream at a distance of $x/x_0=3.06$ (Fig. 2b). This was to allow flow characteristics immediately upstream and downstream of the obstacle to be analyzed. The upstream array coincided with the upstream obstacle face, therefore for obstacle tests, transducers 1–4 were located within the obstacle itself. Likewise, transducers 11–14 were installed in the downstream obstacle face for obstacle tests. This novel approach allowed current velocity to be measured as close as 5 mm from the obstacle faces and 8 mm from the bed surface. The heights were chosen to obtain velocity measurements throughout and above the passing current. The velocity profiles from all transducers were then combined to create a representative vertical velocity profile of the passing current and above ambient fluid. Spatial locations for each transducer are given in Table 2 and visualized in Fig. 2b.

A Lumenera LT425 and LT425C was installed adjacent to the basin wall and above the centre of the false floor, respectively. The LT425 (hereon referred to as “elevation camera”) was located approximately 2.5 m from the basin wall, whilst the LT425C (hereon referred to as “plan camera”), was located approximately 2 m above the false floor. Synchronously, the four-megapixel cameras recorded the complete current front progression, from $x=x_0$ to $x=x_{max}$, at a framerate between 92.6 and 97.9 Hz. To quantify the current data, a spatial calibration and image processing technique similar to Wilson et al. [38] was applied. The first 75 mm from the lock-box (x_{75}) was not included in the photometric analysis for side-view images. This was because opening of the lockbox caused an immediate steep gradient of the current boundary, in which an appropriate head height could not be defined. Illumination of the basin, through sixteen 500 W halogen lamps, was optimized to provide even light distribution on the current, yet minimize reflection from the free surface.

Sixteen tests were conducted in total, with four varying obstacle configurations: smooth substrate with obstacle, smooth substrate with no obstacle, rough substrate with

Table 1 UVP-DUO settings

Setting	Value
Number of transducers	20
Sampling frequency (MHz)	4
Repetitions per profile	32
Sampling period (ms)	15
Total cycle time (s)	1.82
RF gain–US voltage (V)	90
Cycles per pulse	32
Number of channels	128
Distance between channel centres (mm)	1.67
Channel width (mm)	5.92
Measurement window (mm)	5–216.45
Speed of sound (mm s^{-1})	1480
Velocity resolution (mm s^{-1})	2.385
Velocity bandwidth (mm s^{-1})	610.6

Table 2 Spatial location of UVP transducer tips

Transducer #	x/x_0	z/z_0	Transducer #	x/x_0	z/z_0
1	2.45	0.03	11	3.06 ^a	0.03
2	2.45	0.06	12	3.06 ^a	0.06
3	2.45	0.09	13	3.06 ^a	0.09
4	2.45	0.13	14	3.06 ^a	0.13
5	2.45	0.23	15	3.06	0.23
6	2.45	0.33	16	3.06	0.33
7	2.45	0.43	17	3.06	0.43
8	2.45	0.53	18	3.06	0.53
9	2.45	0.63	19	3.06	0.63
10	2.40	0.73	20	2.74	0.73

^aFor obstacle tests where the transducer was within the obstacle, $x/x_0 = 2.69$

obstacle and rough substrate with no obstacle (Table 3). Prior to each test, a Canon 60D reference camera was initiated to record the complete experimental procedure. The UVP console was then simultaneously set to record with a reference stopwatch. Next, the LT425 cameras were set to record, noting the reference time. The prepared slurry was mixed for a further 10 s, and the displacement bucket removed from the lockbox. Next, the slurry was poured into the lockbox and the gate was opened, initiating the turbidity current. Recording of the UVP and LT425 cameras stopped at a minimum of 20 s after the current had passed the obstacle location ($x/x_0 = 2.45$).

Table 3 Experimental parameters

Experiment	Obstacle/substrate condition	ρ_0 (kg m ⁻³)	g' (ms ⁻²)	T (°C)	Volumetric concentration, S_0 (%)
1	No obstacle/smooth bed	1020	0.21	18.5	1.37
2	No obstacle/smooth bed	1040	0.41	19	2.66
3	No obstacle/smooth bed	1060	0.61	20	3.95
4	No obstacle/smooth bed	1080	0.81	22	5.26
5	No obstacle/rough bed	1020	0.22	20.5	1.40
6	No obstacle/rough bed	1040	0.41	20.5	2.68
7	No obstacle/rough bed	1060	0.61	20.5	3.95
8	No obstacle/rough bed	1080	0.8	19.5	5.22
9	Obstacle/smooth bed	1020	0.22	20.5	1.40
10	Obstacle/smooth bed	1040	0.41	21.5	2.69
11	Obstacle/smooth bed	1060	0.61	21	3.96
12	Obstacle/smooth bed	1080	0.81	21.5	5.24
13	Obstacle/rough bed	1020	0.22	21	1.41
14	Obstacle/rough bed	1040	0.41	20	2.67
15	Obstacle/rough bed	1060	0.61	22.5	3.98
16	Obstacle/rough bed	1080	0.8	20.5	5.23

2.1 Analytical methodology

Noise within raw velocity profiles obtained by the UVP transducers was de-spiked using a standard deviation filtering method based on Keevil et al. [43]. The moving, time-wise filter replaced all velocities outside a range of two standard deviations, with the mean of the preceding and proceeding velocity. The standard deviation range was the same as Wilson et al. [44], who found that two standard deviations was the optimal filter width for confined turbidity currents of similar density to the present study. The data from all tests were altered less than 2.47%, therefore considered acceptable.

UVP transducers are not able to record simultaneously, rather they cycle continuously. For the present study, the cycle followed the order of transducer 1–20 with a total cycle time of 1.82 s (Table 1). Therefore, to gain velocity profiles of all transducers at a single representative time, piecewise cubic Hermite time interpolation similar to previous studies was used [44, 45].

For each test, the first five cycles after the current front reached $x/x_0 = 2.29$ ($t_{UVP} = 0$ s, Fig. 5) were used for velocity and turbulence intensity analysis. The range in the present study, which is of similar time range to Eggenhuisen and McCaffrey [26], was chosen after a review of all profiles showed negligible velocity in cycles thereafter. To obtain a detailed view of profile development before and after the obstacle, the two UVP analysis areas were divided into 16 regions of interest: regions 1–8 upstream, regions 9–16 downstream (Fig. 5).

Turbulence intensity was calculated for each transducer in each region of interest, over the five-cycle range, N :

$$I = \sqrt{\sum_{i=1}^N \frac{(u'_i)^2}{N}}, \quad (1)$$

where u' is defined as the velocity component which fluctuates about a mean velocity, \bar{u} , which was calculated using a 3-point moving timewise window:

$$u' = u - \bar{u}. \quad (2)$$

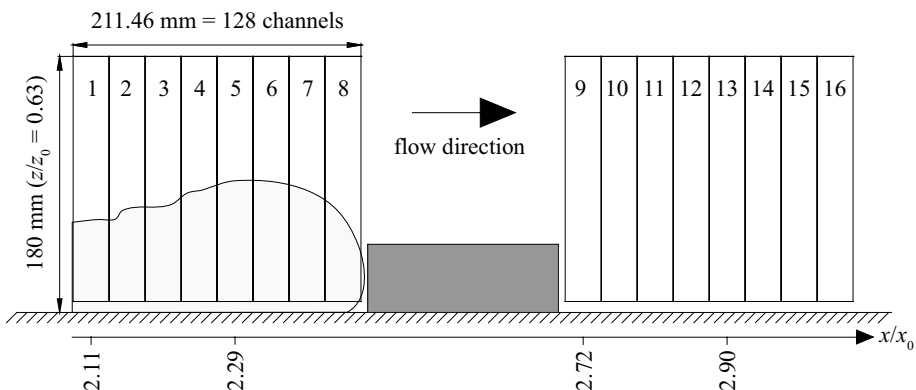


Fig. 5 Overview of the sixteen regions where measured UVP velocity, u , was averaged horizontally within each region to obtain a characteristic velocity for each transducer. All regions had an identical width of 16 channels

To further investigate the velocity profiles, bulk Reynold's, Re_b , and Froude, Fr_b , numbers were calculated. Ellison and Turner [46] derived the now commonly-used moment equations [15, 25, 47] between layer-averaged velocity, U_{ave} , and gravity current height, z_1 :

$$U_{ave} z_1 = \int_0^{z_e} u dz, \quad (3)$$

$$U_{ave}^2 z_1 = \int_0^{z_e} u^2 dz. \quad (4)$$

Equations (3) and (4) were used in the present study to calculate U_{ave} and z_1 . u and u^2 were integrated over height, z , using the trapezoidal rule, where:

$$U_{ave} = \frac{U_{ave}^2 z_1}{U_{ave} z_1} = \frac{\int_0^{z_e} u^2 dz}{\int_0^{z_e} u dz}, \quad (5)$$

$$z_1 = \frac{(U_{ave} z_1)^2}{U_{ave}^2 z_1} = \frac{(\int_0^{z_e} u dz)^2}{\int_0^{z_e} u^2 dz}. \quad (6)$$

The upper boundary of z (z_e) used for integration was set at a value of $z_e/z_0 = 0.43$, which was the approximate height where profiles showed $u \approx 0$. Sequeiros et al. [47] used a similar approximation. The presence of abnormal profiles caused by obstacle interaction made it unsuitable to fit and integrate a typical log-Gaussian curve.

Fr_b , and Re_b were respectively defined as:

$$Fr_b = \frac{U_{ave}}{\sqrt{g' z_1 \cos \theta}}, \quad (7)$$

$$Re_b = \frac{U_{ave} z_1}{\nu}, \quad (8)$$

where specific gravity, g' , was defined as $g' = g(\rho_0 - \rho_a)/\rho_a$, and g represented gravitational acceleration. θ represents the bed slope angle. This form of densimetric Froude number has previously been applied in gravity current studies investigating obstacle interaction [15, 25].

3 Results and discussion

3.1 Visual observations of turbidity current–obstacle interaction

All sixteen tests were found to have visually similar flow characteristics. Upon releasing the lock-box gate, the turbidity current formed and began to radially propagate towards the false floor perimeter. A well-defined, radial head immediately became evident; characterized by a large Kelvin–Helmholtz billow at the rear and small-scale instabilities at the front, as exemplified by Exp. 9 (Fig. 6). The current maintained its radial shape as it approached the obstacle, where lobe and cleft instabilities at the current front appeared

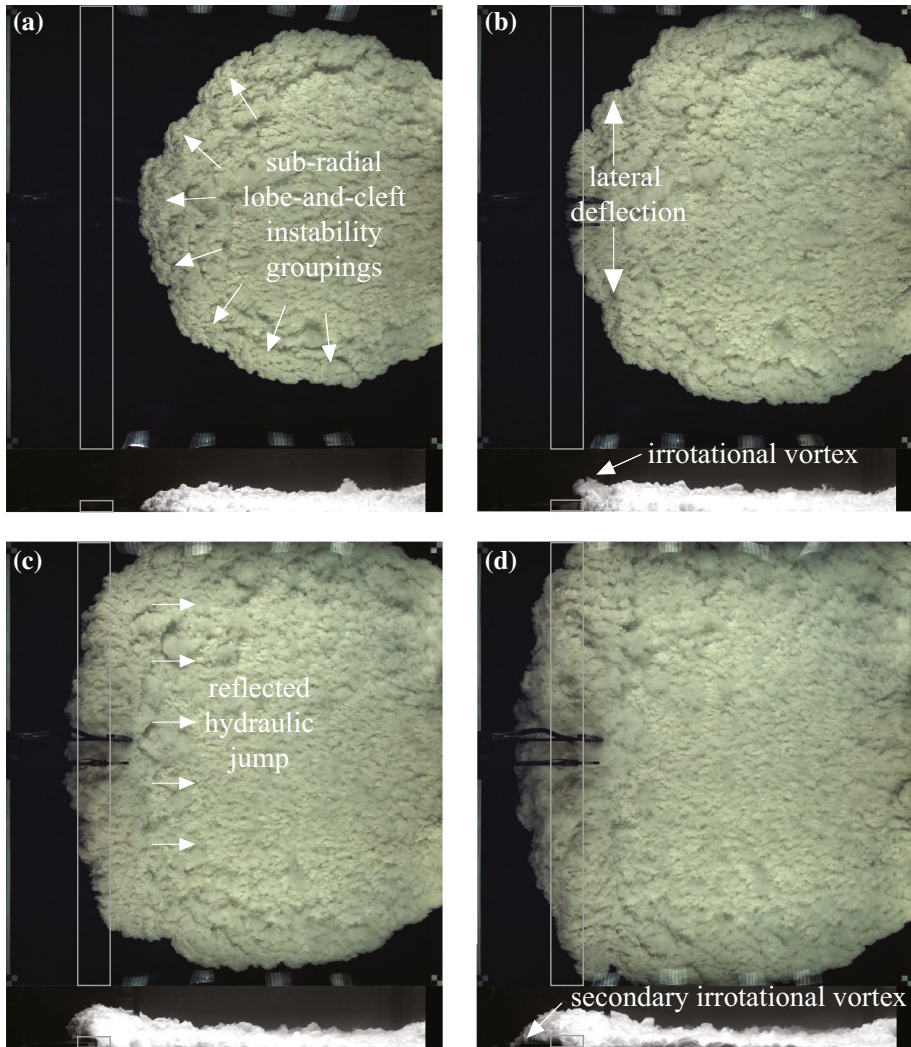


Fig. 6 Plan and side-view images of Exp. 9 at four different stages within the five UVP cycle time range. **a** The current initially expands from the lockbox in a radial motion, where lobe-and-cleft instabilities at front form sub-radial groupings ($t_{UVP}=0$ s); **b** as the current collides with the obstacle, it shears off the top edge in the form of an apparent irrotational vortex ($t_{UVP}=2.89$ s); **c** the current is partially reflected as a hydraulic jump ($t_{UVP}=6.59$ s); **d** a secondary vortex is formed as the current shears off the downstream end of the obstacle ($t_{UVP}=9.10$ s). For clarity, the obstacle boundary adopted for photometric measurement is outlined in grey, where the elevation-view obstacle boundary represents the analyzed cross-section along the basin centreline

to group into sub-radial regions (Fig. 6a). For unobstructed tests, the current appeared to propagate at a constant rate until it spilled over the false floor. When considering that turbidity currents typically transition from an initial constant-velocity slumping phase to a self-similar phase at a distance of 5–10 lockbox lengths (i.e. past the physical extent

of the false floor for the present study), it was assumed the unobstructed current stayed within the slumping phase throughout the analysis area [1].

For obstacle tests, when the current reached the obstacle face it was deflected both vertically, as a jet, and laterally towards the false floor edges (Fig. 6b). It was also partially reflected upstream towards the lockbox in the form of a hydraulic jump—a common feature of gravity current-obstacle interaction [16, 48–50]. An irrotational vortex, similar to that observed by Wilson et al. [51], was observed to form as the current sheared off the upstream obstacle face and travelled over the obstacle. The vertical jet continued to expand until it reached a maximum height, where it subsequently collapsed once gravitational forces exceeded momentum forces of the jet (Fig. 6c). Lateral movements along the obstacle face appeared to dominate longitudinal movements, causing the radial head to become more linear in shape. The current then sheared off the downstream obstacle edge, creating a secondary irrotational vortex, and reattached with the bed (Fig. 6d). As the current reattached to the bed, the head began to re-establish and a large instability at the rear became significant. The body of the current continued to flow over the obstacle in an apparent supercritical manner, feeding the instability at the back of the head. Meanwhile the reflected hydraulic jump continued to propagate upstream.

3.2 Velocity profiles

Velocity measurements, u , from each transducer were spatially averaged for each of the 16 regions of interest. u was then temporally averaged over the five transducer cycles selected for analysis. Linear interpolation was applied for each dataset to construct a vertical profile. The velocity at the bed was set to zero, assuming a no-slip boundary condition. Figure 7a, b show upstream and downstream velocity profiles for no-obstacle tests, respectively. In

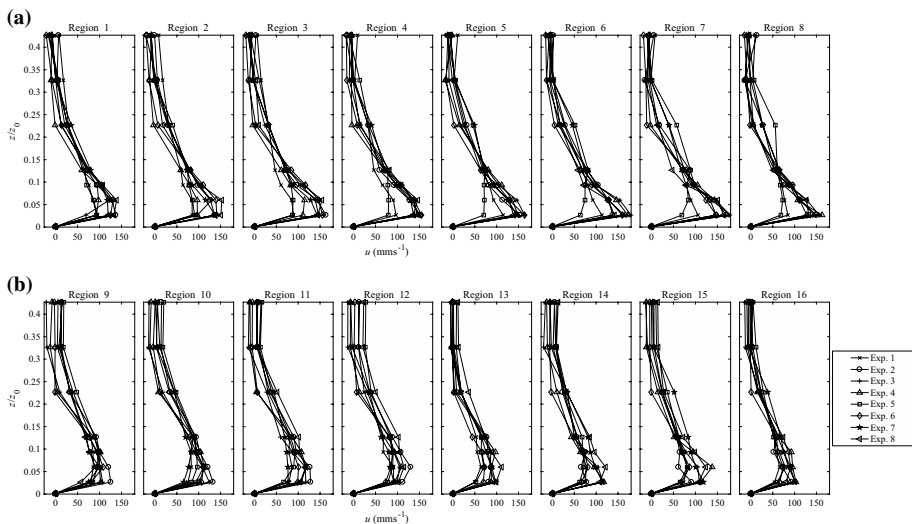


Fig. 7 Vertically non-dimensionalized velocity profiles of the passing turbidity current for no-obstacle tests, showing a characteristic log-Gaussian curve. **a** Shows profiles for upstream regions 1–8, whilst, **b** shows profiles for downstream regions 9–16. u obtained from transducers 8, 9, 18 and 19 were excluded due to the negligible velocity above the current profile

general, all profiles can be seen to resemble the typical log-Gaussian curve; where u_{max} occurs at a mean height of $z_{max}=z/z_1=0.20$ for upstream profiles and 0.25 for downstream profiles. This shows good agreement with Kneller et al. [23] and Baas and Best [52]. The difference in height between upstream and downstream profiles is likely related to minor flow interference by the upstream UVP rack. Some experiments also showed visual increase in head height, which may have also contributed to the difference. Upstream no-obstacle profiles had a mean u_{max} of 133 mm s^{-1} and range of $73\text{--}181 \text{ mm s}^{-1}$. Subsequently, downstream no-obstacle profiles had a mean u_{max} of 99 mm s^{-1} and range of $64\text{--}138 \text{ mm s}^{-1}$. This implies that the profiles experience a gradual decrease in velocity over distance, x ; however, Fig. 7 shows a visible decrease in u_{max} between region 8 (measured by upstream UVP rack) and region 9 (measured by downstream UVP rack), suggesting that the upstream UVP rack had some influence on flow within regions 9 through to 16. However, regions 9–16 showed a more gradual decrease in velocity than regions 8–9, suggesting any influence from the UVP racks was not localized and did not significantly affect the current development. In general, u_{max} was found to be proportional with ρ_0 . This is exemplified between experiments 1 and 5. Upstream profiles showed the Gaussian-shaped jet region to transition to negative velocities above the current boundary—a feature similar to other studies [15, 25, 47]. This suggests the presence of a typical reverse ambient flow above the current. Interestingly, this was only present in experiments 3, 4, 6 and 7 for downstream profiles (Fig. 7b). Region 15, and to a degree region 14, showed a decrease in velocity for experiment 2 at $z/z_0=0.06$. A review of velocity profile data for transducer 12 showed a localized area of constant velocity in this region, suggesting the apparent velocity decrease was due to instrument noise. A check on other experiments in this area showed no similar occurrence, suggesting it was isolated to experiment 2. Lastly with respect to substrate, there was no significant difference in u between rough and smooth bed conditions.

The upstream and downstream velocity profiles of obstacle tests (Fig. 8a, b, respectively) show a remarkable difference. On approach to the obstacle (region 8), the profiles generally showed a transition from the hybrid log-Gaussian distribution to a more singular Gaussian distribution. This resulted in u_{max} gradually increasing in height from a mean of $z_{max}/z_0=0.09$ in region 1 to a mean of $z_{max}/z_0=0.19$ in region 8, which is above the obstacle height (Fig. 8a). This follows the conservation of mass, where a local deceleration in flow must be balanced with an increase in vertical (in the form of a jet) and lateral spread, which was evident in all tests (Fig. 6b). It also agrees with the visible vortex, which accelerates over the top edge of the obstacle. Below z_{max} , the velocity profile diminished rapidly to a minimum or in most cases to a negative velocity (experiments 10–13 and 15–16). Interestingly, this was more evident for experiments with higher ρ_0 , a trend also seen by the confined experiments of Yaghoubi et al. [15]. This demonstrates the presence of a stagnant/weak recirculation region directly upstream of the obstacle, which is further exemplified in Fig. 9a—showing spatial plots of the velocity field upstream and downstream of the obstacle for the first UVP cycle of experiment 12. It also agrees well with visual observations of a reflected turbidity current bore, where a degree of reverse flow within the current body, upstream of the obstacle, is expected. Such a region was also present in Sequeiros et al. [47], who studied confined density currents interacting with a 45° obstruction. Minimal velocity in this region is likely to cause a localized increase in rate of deposition; hence reduction in concentration, as exemplified by previous studies [14, 53]. Velocity profiles also showed a considerably greater range in u_{max} ($18\text{--}129 \text{ mm s}^{-1}$) than no-obstacle profiles. This increase in distortion was also seen by Yaghoubi et al. [15] and Oshaghi et al. [25], where the former attributed this phenomenon to the interaction of inertial forces with an adverse pressure gradient existing due to the obstacle.

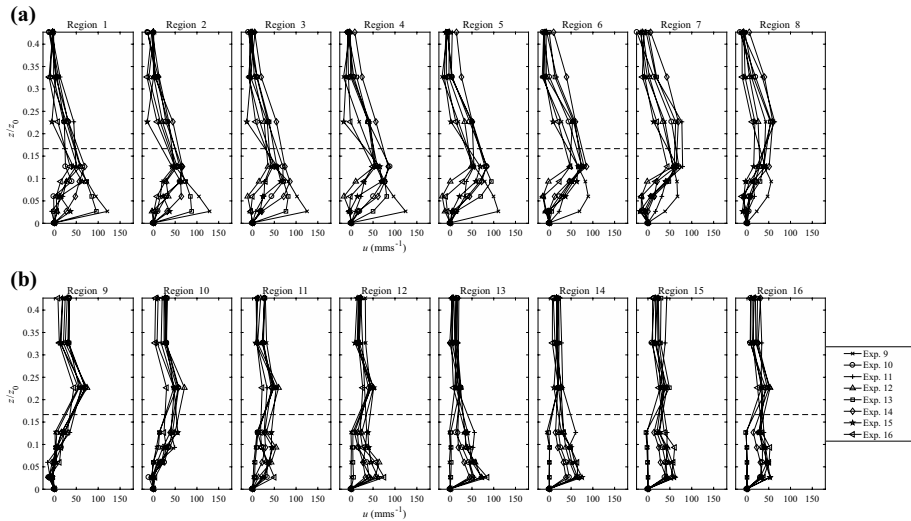


Fig. 8 Vertically non-dimensionalized velocity profiles of the passing turbidity current for obstacle tests, where the obstacle causes the general profile shape to deviate from the typical log-Gaussian profile. **a** Shows profiles for upstream regions 1–8, whilst **b** shows profiles for downstream regions 9–16. The obstacle height is indicated as a dashed line. u obtained from transducers 8, 9, 18 and 19 were excluded due to the negligible velocity above the current profile

Downstream of the obstacle, velocity profiles appeared to mirror upstream profiles, where initially the profile was of a Gaussian shape, progressing to a log-Gaussian shape (Fig. 8b). u_{max} was located at a mean height of $z_{max}/z_0 = 0.23$ in region 9, and decreased to a mean height of $z_{max}/z_0 = 0.16$ in Region 16 downstream. This signifies the complete re-attachment of the current to the bed. A localized area of minimal/negative velocities was present in regions 9–11 near the bed (Fig. 8b). This can be explained by the shearing of the current over the top edge of the obstacle, which was visually seen to cause formation of a counter-clockwise irrotational vortex. This was further exemplified in Fig. 9b. Yaghoubi et al. [15] also found a recirculation region near the bed, downstream of the obstacle. However, it was considerably smaller in height and distance. This is likely due to the less-streamline, rectangular obstacle shape in the present study than the triangular obstacle used by the former study; hence shearing is encouraged over the downstream edge, forming an instability. Yaghoubi et al. [15] found this secondary recirculation region to decrease in size with increasing current concentration, however the same conclusion cannot be made for the present study. An intriguing aspect was the formation of a secondary local velocity maximum, prevalent in regions 11–12 and 15–16 for runs 9–12. An explanation may be that as the current collapsed over the rear obstacle edge, the lower maximum was driven by buoyancy forces of the accelerating head, whilst the upper maximum was caused by the collapse of the jet; where a layer of reverse flow existed between (Fig. 9b). u_{max} in the downstream region had a mean of 52 mm s^{-1} , which was noticeably less than mean upstream u_{max} (68 mm s^{-1}). This shows the obstacle was effective in reducing maximum velocities, by approximately 48% of mean downstream u_{max} of no-obstacle experiments. Similar to no-obstacle tests, u_{max} generally increased with ρ_0 , however the differences in profiles across different ρ_0 are seen to be minimal. There was also no strong relationship between u_{max} and substrate condition.

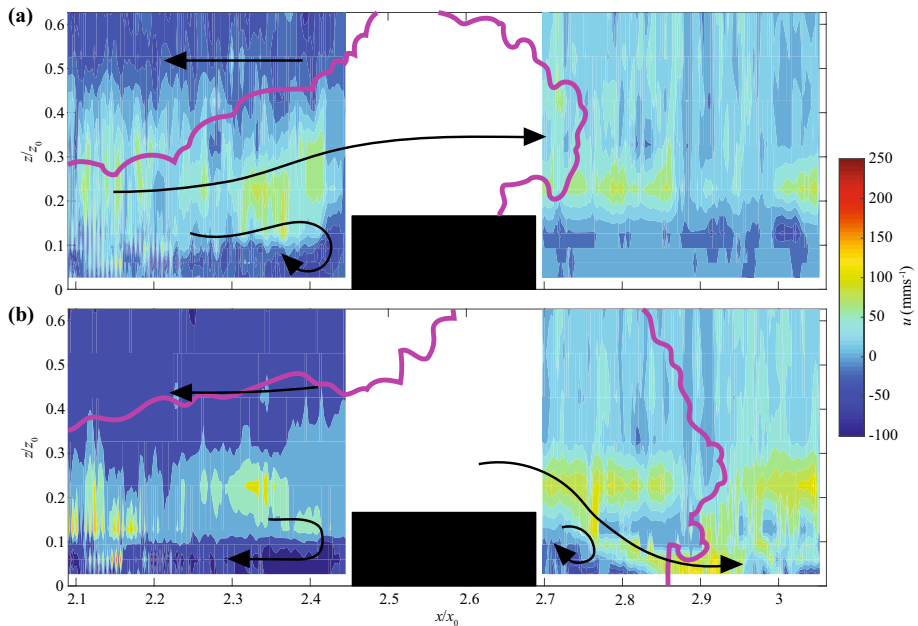


Fig. 9 Spatial velocity contour plot of Exp. 12. Velocity measurements from each transducer were arranged spatially, and interpolated to create a contour map. The corresponding head location, obtained from photometric analysis, is schematically plotted as a solid magenta line style. **a** The second UVP cycle used for the analysis, which shows that as the current propagates over the obstacle, a basal region of reflected/recirculated flow is present immediately upstream of the obstacle. **b** The third UVP cycle used for analysis, which shows that as the head propagates downstream of the obstacle, a secondary recirculation region ($x/x_0=2.7\text{--}2.8$) is present immediately downstream of the obstacle. Both cycles show that a reverse ambient bore is present above the current

An outline of the turbidity current head, obtained from the photometric data, was plotted over the UVP velocity profiles for the equivalent UVP cycle time step of the UVP cycles shown in Fig. 9a, b. It is demonstrated that the photometric boundaries show some agreement with the UVP data obtained, particularly where the current reattaches with the bed after the obstacle in Fig. 9b. The apparent differences in perceived current boundary between the two measurement techniques upstream of the obstacle are likely due to the time-wise averaging of the transducer profiles. These differences suggest future work is needed in developing more comprehensive methods for integrating the quantitative results of the two techniques.

An interesting observation between obstacle and no-obstacle tests was that the reduction in layer-averaged velocity, U_{ave} , between upstream and downstream regions was comparable (Fig. 10a, b, respectively). However, the range of U_{ave} for obstacle tests ($14\text{--}103\text{ mm s}^{-1}$) was clearly less than that of no obstacle tests ($49\text{--}131\text{ mm s}^{-1}$). This suggests that the significant change in local velocity profile structure seen as the current propagates over the obstacle (Fig. 8), is somewhat independent of U_{ave} . Figure 10a also shows that U_{ave} increased with increasing ρ_0 , however this was not discernible for obstacle tests (Fig. 9b). Similar to the measured velocity profiles, there is negligible evidence that the substrate condition is related to U_{ave} . This was highlighted through the mean fit of U_{ave} for smooth and rough tests (Fig. 10a, b), which in general, appeared to fluctuate around each

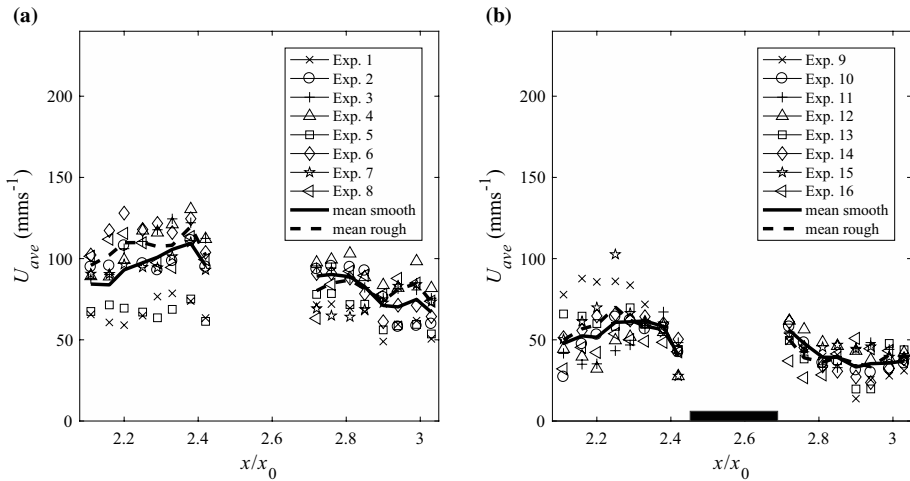


Fig. 10 Depth-averaged velocity, U_{ave} , calculated for regions 1–16 and plotted as a function of x/x_0 . **a** Shows profiles for no-obstacle experiments, whilst **b** shows profiles for obstacle experiments, where the obstacle location is shown in bold. For both plots, the mean U_{ave} values for smooth and rough tests are shown as the solid and dashed line, respectively

other with no clear trend. An exception is shown in Fig. 10a, where mean U_{max} was greater for rough tests in regions 1–8. However, given this was not shown for obstacle tests or in other regions, and is contrary to previous studies which show substrate roughness reduces velocity [33], further testing is needed to confirm the trend's validity.

3.3 Turbulence intensity profiles

Using Eq. (1), I was calculated for each transducer, over each region, for all tests. Figure 11a shows that for regions 1–8, intensity profiles of no-obstacle experiments had between 1 and 2 turbulence intensity maxima, where the lowest local maximum was generally below $z/z_0=0.1$. The largest maximum in each profile ranged between $I_{max}=13\text{--}43\text{ mm s}^{-1}$, with an average of 22 mm s^{-1} . In regions 9–16, this range increased to $I_{max}=11\text{--}70\text{ mm s}^{-1}$, with a slightly higher average of 25 mm s^{-1} (Fig. 11b). These values are in agreement with the vertical turbulence intensities measured by Eggenhuisen and McCaffrey [26], who tested currents of similar density in confined conditions. The average height of I_{max} in regions 1–8 ($z/z_0=0.16$) decreased to 0.045 in regions 9–16. I_{max} is expected to be greatest near the bed, where the current experiences the greatest change in velocity, hence the highest shear stress and turbulence. As also expected, intensities tended to be higher for experiments of greater ρ_0 , which is exemplified in regions 7–11.

For obstacle experiments, the presence of two intensity maxima was visibly more evident than no-obstacle tests. Figure 12a shows that for regions upstream of the obstacle, the lower turbulence intensity maximum tended to occur below the obstacle height ($z/z_0=0.17$), whilst the upper maximum occurred between $z/z_0=0.2\text{--}0.6$. I_{max} in regions 1–8 ranged between $10\text{ and }52\text{ mm s}^{-1}$, with a mean of 24 mm s^{-1} . In regions 9–16 the range decreased to $7\text{--}33\text{ mm s}^{-1}$, with a mean of 18 mm s^{-1} (Fig. 12b). This decrease in mean I_{max} of 25% shows that the obstacle had an effect on reducing downstream

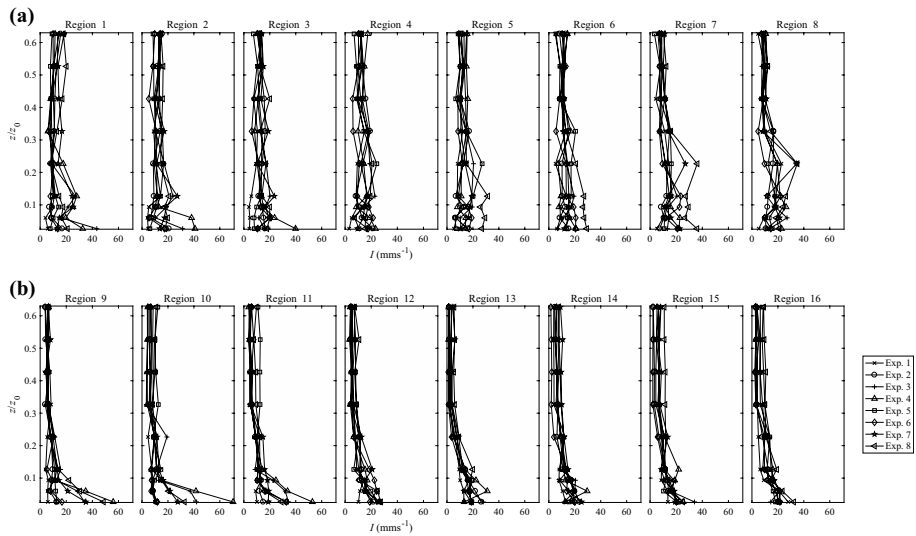


Fig. 11 Vertically non-dimensionalized turbulence intensity (I) profiles of the passing turbidity current for no-obstacle tests. **a** Shows profiles for upstream regions 1–8, whilst **b** shows profiles for downstream regions 9–16

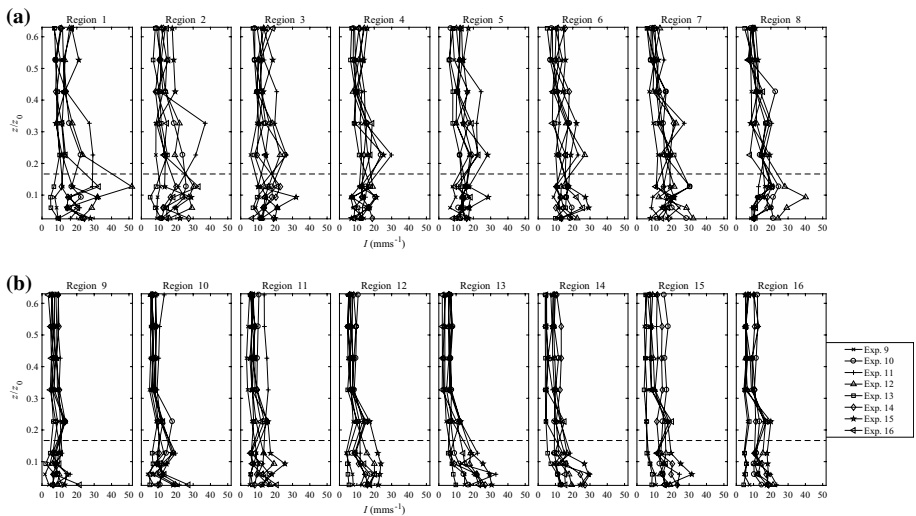


Fig. 12 Vertically non-dimensionalized turbulence intensity (I) profiles of the passing turbidity current for obstacle tests. **a** Shows profiles for upstream regions 1–8, whilst **b** shows profiles for downstream regions 9–16. The obstacle height is shown as a dashed line

maximum turbulence, contrary to no-obstacle experiments which showed a slight increase in mean I_{max} . This also agrees well with Eggenhuisen and McCaffrey [26], who found that the height and intensity of turbulence intensity maximum is controlled by the obstacle, rather than upstream flow conditions. Overall, turbulence intensity profiles of obstacle

experiments were seen to be more scattered than no-obstacle experiments. This was particularly evident within the upper extent of profiles in upstream regions 1–8. It was likely related to the interaction of the forward propagating flow with the reflected hydraulic jump, and also the vertically expanding jet.

In both obstacle and no-obstacle experiments, it was found that substrate condition had no discernible effect on the magnitude of intensity maxima. This contrasts with Eggenhuisen and McCaffrey [26] who found the presence of a 5 mm high rough substrate to increase the local intensity maximum near the bed. It also contrasted with Stagnaro and Bolla Pittaluga [54], who showed that the presence of a 3 mm high rough substrate caused velocity intensity near the bed in confined saline currents to diminish and maximum velocity height to increase. However, the absolute roughness height of the substrates used in these studies is notably higher than the present study (0.85 mm), which may explain the dissimilarity. No-obstacle tests showed that in regions 1–8, I_{max} had a mean height of $z/z_0=0.16$, whereas downstream $z/z_0=0.04$. To the contrary, obstacle tests showed that the mean height of I_{max} increased from $z/z_0=0.09$ to 0.17 over the obstacle. This increase in I_{max} height, paired with the tendency of obstacle tests to show more variation in I_{max} in the upper regions of the profile suggests that although the obstacle may have reduced intensity maxima, it encouraged small-scale turbulence at the upper regions of the current. This promotes mixing and entrainment of ambient fluid, which agrees well with visual observations of the jet expansion and deflection. However, future studies are warranted to confirm the recurrence of local maxima, given the uncertainty introduced by the temporal resolution of the UVP console (total transducer cycle time = 1.82 s). Present UVP technology introduces a trade-off between spatial and temporal resolution. Although both are important, spatial resolution took precedence in the present study, given the interest in investigating the spatial regions over the obstacle. To overcome this, future studies may involve the use of multiple UVP consoles—at a significant cost—or focus on fewer spatial regions, with more repeat tests.

3.4 The role of unconfinement and substrate roughness on turbidity current–obstacle interaction

To further investigate current flow characteristics, Eqs. (7) and (8) were used to calculate bulk Froude, Fr_b and bulk Reynolds numbers, Re_b , respectively. Although the non-dimensional parameters were calculated locally for each region, they are considered a bulk representation, given that the current velocities and heights were averaged over time for each region. The Reynolds and Froude analysis, along with the qualitative insights into the current propagation characteristics over the obstacle, such as the recirculation regions and vortices formed, provide a basis upon which numerical models of unconfined turbidity currents interacting with an obstacle may be compared. Figure 13a shows Fr_b decreased from a subcritical range of 0.4–0.6 in region 1 to a range of 0.3–0.5 in region 16, for no-obstacle tests. This agrees well with the findings of confined studies [15, 25]. It also has considerable overlap to the range of Wilson et al. [51] (0.38–0.64), who studied confined currents with identical initial densities, bed slope and ambient fluid height to the present study. This suggests that stream-wise Froude number is not significantly affected by the unconfined, lateral propagation of the current. Experiment 6 is shown to be an exception in regions 1–8, where Fr_b reached values closer to unity. This is due to u in Exp. 6 being amongst the higher readings from all experiments, combined with a lower than average z_1 for the first 8 regions. The most probable explanation for this anomaly is that it is related to the

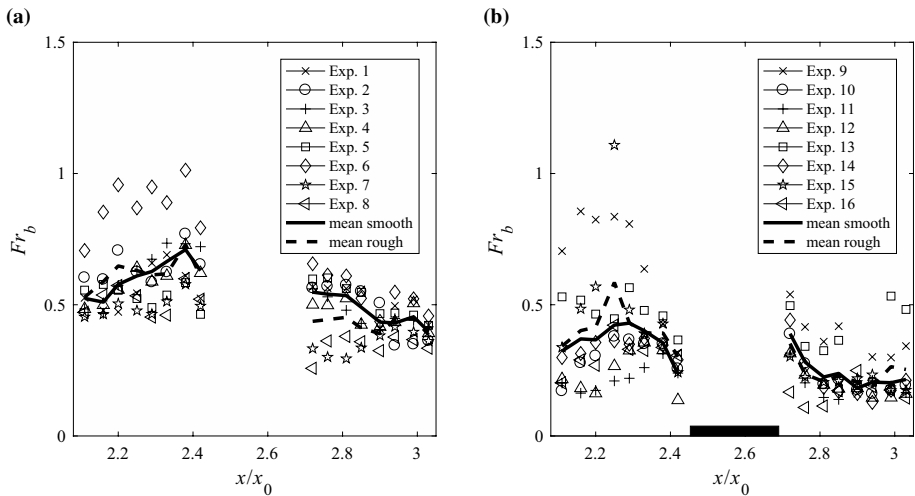


Fig. 13 Bulk Froude number, Fr_b , calculated for regions 1–16 and plotted as a function of x/x_0 . **a** Shows profiles for no-obstacle experiments, whilst **b** shows profiles for obstacle experiments, where the obstacle location is shown in bold. For both plots, the mean Fr_b values for smooth and rough tests are shown as the solid and dashed line, respectively

initiation process of the current, where human error may have been introduced; however, as described in Sect. 2, an effort was made to minimize introduced errors. Interestingly, experiments with higher ρ_0 were found to have a lower Fr_b value. There was also no evident relationship between substrate condition and Fr_b . The obstacle experiments showed that for most experiments, Fr_b fell in the lower range of approximately 0.1–0.4 (Fig. 13b). However, Fr_b was more scattered than no-obstacle experiments, showing an overall greater range. This agrees well with velocity and turbulence intensity profiles, which showed that the obstacle generally caused a reduction in mean maxima values in regions 1–8, yet caused an overall greater range of values. The upstream Fr_b values are comparable to Yaghoubi et al. [15] and Oshaghi et al. [25], however, they are a degree lower than the inter-quartile ranges of Wilson et al. [51] (0.21–0.52), who used an obstacle of identical dimensions to the present study.

Bulk Reynolds, Re_b , showed similar characteristics to Fr_b , where obstacle experiments had a larger range, yet lower mean than no-obstacle experiments—driven by a decrease in U_{ave} . No-obstacle experiments showed Re_b to be in the approximate range of 2800–6600 (Fig. 14a). This range was found to be slightly lower than the bulk Reynolds numbers reported in the confined studies of Nogueira et al. [32] (3800–8200), who tested currents of similar initial specific gravity to the present study (0.17–0.61). Obstacle experiments showed Re_b to vary from a laminar state of approximately 500 to turbulent regimes of 5100 (Fig. 14b). Similar to Fr_b , Re_b appeared to have no evident relationship with substrate condition. The substrate condition, in general, was shown to have negligible effect on all stream-wise flow characteristics—specifically turbulence intensity and velocity maxima—contrary to other studies who adopted similar roughness-specific gravity scales. Nogueira et al. [32], who studied confined gravity currents passing over a 2.9 mm high bed roughness, found the current front velocity to decrease with increasing bed roughness. The most likely reason such a decrease was not found in the present study was due to the smaller substrate roughness height, hence drag forces were not dissimilar to a smooth bed.

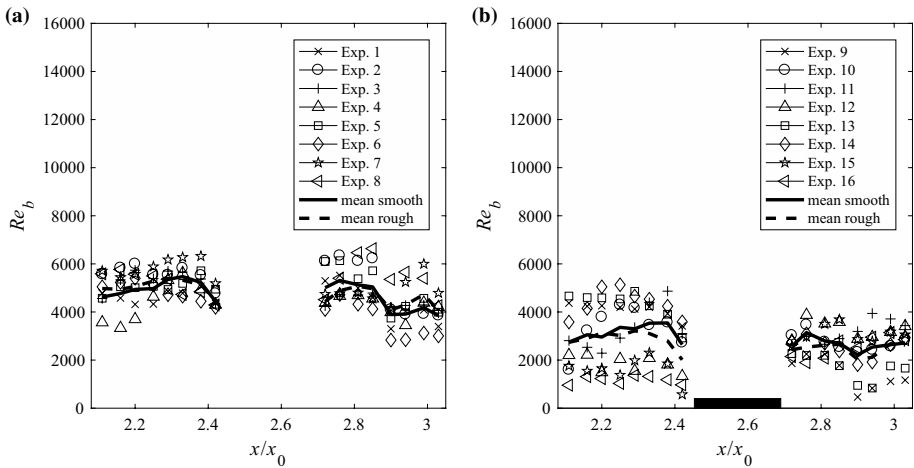


Fig. 14 Bulk Reynolds number, Re_b , calculated for regions 1–16 and plotted as a function of x/x_0 . **a** Shows profiles for no-obstacle experiments, whilst **b** shows profiles for obstacle experiments, where the obstacle location is shown in bold. For both plots, the mean Re_b values for smooth and rough tests are shown as the solid and dashed line, respectively

However, La Rocca et al. [29] tested unconfined currents over a substrate with a roughness height of 0.7 mm and initial specific gravity of 0.14–0.24, also showing the rough substrate decreased velocity. They found the current experienced two phases of velocity: an initial inertial-buoyant phase where velocity increased and became steady, followed by a secondary phase where velocity decreased gradually. They found that the substrate decreased velocities most notably in this second stage. In the present study, currents only experienced the inertial-buoyant slumping phase, where velocities were constant for no-obstacle tests. The present study also adopted a bed slope of 2% compared to a flat bed in La Rocca et al. [29] and Nogueira et al. [32]; where the slope causes momentum forces due to gravity to dominate resistance from the bed, thus may reduce the retarding effect of the bed roughness. Further research is needed, adopting a greater range of roughness heights to determine when roughness noticeably plays a role in reducing current velocity and increasing near-bed turbulence intensity.

The unobstructed velocity profiles confirmed that a lock-released, unconfined current has the classical log-Gaussian velocity distribution. The obstructed velocity profiles, however, showed that vertical velocity distribution is altered considerably as it propagates over the obstacle. The two key differences to no-obstacle runs was the presence of a recirculation region directly upstream and downstream of the obstacle. The downstream recirculation region, related to shearing of the current over the obstacle top, was confirmed through visual analysis of the irrotational vortex, which formed over the downstream obstacle edge. The upstream recirculation region was caused by deflection of the current at the upstream obstacle face. An important aspect to note is that these findings are not dissimilar to those of confined studies involving obstacles [15, 25, 47]. This shows that ultimately, confinement doesn't significantly alter the predicted internal flow structure in the context of a stream-wise, two-dimensional cross-section of unconfined flow. However, visual observation showed that current deflection from the obstacle had a lateral component (Fig. 6b). It cannot be ruled out that these lateral characteristics may affect the extent of the stream-wise recirculation region, hence influence sediment detrainment mechanisms at the foot of

the obstacle. This is important, as it may provide insights into the lateral spreading of sedimentation upstream of unconfined, linear obstacles—practical knowledge which is needed to better understand the usefulness of a linear obstacle as a barrier to unconfined flow. Therefore, more work is required to quantify the internal flow structure of lateral components to understand how they may be related to stream-wise structure.

When considering the efficiency of the obstacle to reduce current velocity within the analysis area, the profiles for obstacle tests showed mean u_{max} was 48% less than unobstructed experiments, downstream of the obstacle location. Similarly, mean downstream I_{max} was found to be 28% less for obstacle experiments, yet obstacle experiments showed turbulence activity was more spread throughout the vertical profile. This suggests that the obstacle is effective in reducing current turbulence and velocity, yet it distributes fine-scale turbulence, creating a thicker mixing layer. However, this study was focused on the characteristics observed in the immediate regions of the obstacle. Further research is needed on the development of the current head once it has completely re-established, to gain a better understanding on the whole-of-life effects of the obstacle.

4 Conclusions

The present study investigated the velocity and turbulence structure of an unconfined, lock-exchange turbidity current interacting with a linear, rectangular obstacle. Key velocity and turbulence characteristics were identified, and compared with confined studies over a range of different initial density and substrate conditions. The influence of lateral unconfinement on the stream-wise velocity was discussed, along with the efficiency of the obstacle to act as a barrier to flow. The stream-wise characteristics of the current were comparable to confined studies, suggesting unconfinement has minor influence.

The novel placement of transducers within the obstacle face showed that as the current propagates over the obstacle, a recirculation region of negative velocities develops immediately upstream and downstream, and that an overlying ambient bore is present. This agrees well with the findings of previous confined studies, showing that in general, the stream-wise flow structures are independent of confinement. The unobstructed currents formed a classical log-Gaussian velocity profile, which for obstructed experiments, was transformed into a more Gaussian-like shape over the obstacle. Maximum velocity and turbulence intensity downstream of the obstacle location was found to be 48% and 28% less than for unobstructed experiments. This showed that the obstacle was effective in reducing current velocity and turbulence for the immediate region of the obstacle. However, the greater observed variance in height and magnitude of velocity and intensity maxima for obstructed experiments suggests that the velocity distribution throughout the current height became less stratified, promoting mixing and entrainment of ambient fluid in the regions immediately adjacent to the obstacle face. Future research of the velocity and turbulence structure during the re-establishment stage after the obstacle is needed to confirm the whole-of-life effects the obstacle has on the current.

Based on our work, we identify comparison of lateral flow structure along the obstacle face between the two confinement scenarios as important future research. Furthermore, there is merit in investigating if local sedimentation is affected by confinement condition.

Acknowledgements We would like to thank Trevor Patrick, Geoff Kirby and Jim Luo for their help in constructing and installing required experimental components.

Compliance with ethical standards

Conflict of interest The authors declare that they have no conflict of interest.

References

1. Meiburg E, Kneller B (2010) Turbidity currents and their deposits. *Annu Rev Fluid Mech* 42(1):135–156. <https://doi.org/10.1146/annurev-fluid-121108-145618>
2. Xu JP, Noble MA, Rosenfeld LK (2004) In-situ measurements of velocity structure within turbidity currents. *Geophys Res Lett* 31(9):L09311. <https://doi.org/10.1029/2004GL019718>
3. Heezen BC, Ewing M (1952) Turbidity currents and submarine slumps, and 1929 grand banks earthquake. *Am J Sci* 250(12):849–873. <https://doi.org/10.2475/ajs.250.12.849>
4. Krause DC, White WC, Piper DJW, Heezen BC (1970) Turbidity currents and cable breaks in the western New Britain Trench. *Geol Soc Am Bull* 81(7):2153–2160. [https://doi.org/10.1130/0016-7606\(1970\)81%5b2153:TCACBI%5d2.0.CO;2](https://doi.org/10.1130/0016-7606(1970)81%5b2153:TCACBI%5d2.0.CO;2)
5. Hsu SK, Kuo J, Lo CL, Tsai CH, Doo WB, Ku CY, Sibuet JC (2008) Turbidity currents, submarine landslides and the 2006 Pingtung earthquake off SW Taiwan. *Terr Atmos Ocean Sci* 19(6):767–772. [https://doi.org/10.3319/TAO.2008.19.6.767\(PT\)](https://doi.org/10.3319/TAO.2008.19.6.767(PT))
6. Carter L, Milliman JD, Talling PJ, Gavey R, Wynn RB (2012) Near-synchronous and delayed initiation of long run-out submarine sediment flows from a record-breaking river flood, offshore Taiwan. *Geophys Res Lett* 39(12):L12603. <https://doi.org/10.1029/2012GL051172>
7. Cattaneo A, Babonneau N, Ratzov G, Dan-Unterseh G, Yelles K, Bracène R, Mercier de Lépinay B, Boudiaf A, Déverchère J (2012) Searching for the seafloor signature of the 21 May 2003 Boumerdès earthquake offshore central Algeria. *Nat Hazards Earth Syst Sci* 12(7):2159–2172. <https://doi.org/10.5194/nhess-12-2159-2012>
8. Pope EL, Talling PJ, Carter L (2017) Which earthquakes trigger damaging submarine mass movements: insights from a global record of submarine cable breaks? *Mar Geol* 384:131–146. <https://doi.org/10.1016/j.margeo.2016.01.009>
9. Bruschi R, Bughi S, Spinazzè M, Torselletti E, Vitali L (2006) Impact of debris flows and turbidity currents on seafloor structures. *Norw J Geol* 86(3):317–336
10. Testik FY, Yilmaz NA (2015) Anatomy and propagation dynamics of continuous-flux release bottom gravity currents through emergent aquatic vegetation. *Phys Fluids* 27(5):056603. <https://doi.org/10.1063/1.4919783>
11. Ho H-C, Lin Y-T (2015) Gravity currents over a rigid and emergent vegetated slope. *Adv Water Resour* 76:72–80. <https://doi.org/10.1016/j.advwatres.2014.12.005>
12. Schleiss AJ, Franca MJ, Juez C, De Cesare G (2016) Reservoir sedimentation. *J Hydraul Res* 54(6):595–614. <https://doi.org/10.1080/00221686.2016.1225320>
13. Oehy C, De Cesare G, Schleiss AJ (2010) Effect of inclined jet screen on turbidity current. *J Hydraul Res* 48(1):81–90. <https://doi.org/10.1080/00221680903566042>
14. Oehy C, Schleiss AJ (2007) Control of turbidity currents in reservoirs by solid and permeable obstacles. *J Hydraul Eng* 133(6):637–648. [https://doi.org/10.1061/\(ASCE\)0733-9429\(2007\)133:6\(637\)](https://doi.org/10.1061/(ASCE)0733-9429(2007)133:6(637))
15. Yaghoubi S, Afshin H, Firoozabadi B, Farizan A (2017) Experimental investigation of the effect of inlet concentration on the behavior of turbidity currents in the presence of two consecutive obstacles. *J Waterw Port Coast Ocean Eng* 143(2):04016018. [https://doi.org/10.1061/\(ASCE\)WW.1943-5460.0000358](https://doi.org/10.1061/(ASCE)WW.1943-5460.0000358)
16. Gonzalez-Juez E, Meiburg E (2009) Shallow-water analysis of gravity-current flows past isolated obstacles. *J Fluid Mech* 635:415–438. <https://doi.org/10.1017/S0022112009007678>
17. Gonzalez-Juez E, Meiburg E, Constantinescu G (2009) Gravity currents impinging on bottom-mounted square cylinders: flow fields and associated forces. *J Fluid Mech* 631:65–102. <https://doi.org/10.1017/S0022112009006740>
18. Tokyay T, Constantinescu G, Gonzalez-Juez E, Meiburg E (2011) Gravity currents propagating over periodic arrays of blunt obstacles: effect of the obstacle size. *J Fluid Struct* 27(5–6):798–806. <https://doi.org/10.1016/j.jfluidstructs.2011.01.006>
19. Tokyay T, Constantinescu G, Meiburg E (2012) Tail structure and bed friction velocity distribution of gravity currents propagating over an array of obstacles. *J Fluid Mech* 694:252–291. <https://doi.org/10.1017/jfm.2011.542>
20. Nasr-Azadani MM, Meiburg E (2014) Turbidity currents interacting with three-dimensional seafloor topography. *J Fluid Mech* 745:409–443. <https://doi.org/10.1017/jfm.2014.47>

21. Tokyay T, Constantinescu G (2015) The effects of a submerged non-erodible triangular obstacle on bottom propagating gravity currents. *Phys Fluids* 27(5):056601. <https://doi.org/10.1063/1.4919384>
22. Altinakar MS, Graf WH, Hopfinger EJ (1996) Flow structure in turbidity currents. *J Hydraul Res* 34(5):713–718. <https://doi.org/10.1080/00221689609498467>
23. Kneller B, Bennett S, McCaffrey WD (1999) Velocity structure, turbulence and fluid stresses in experimental gravity currents. *J Geophys Res Oceans* 104(C3):5381–5391. <https://doi.org/10.1029/1998JC900077>
24. Choux CMA, Baas JH, McCaffrey WD, Haughton PDW (2005) Comparison of spatio-temporal evolution of experimental particulate gravity flows at two different initial concentrations, based on velocity, grain size and density data. *Sediment Geol* 179(1–2):49–69. <https://doi.org/10.1016/j.sedgeo.2005.04.010>
25. Oshaghi MR, Afshin H, Firoozabadi B (2013) Experimental investigation of the effect of obstacles on the behavior of turbidity currents. *Can J Civil Eng* 40(4):343–352. <https://doi.org/10.1139/cjce-2012-0429>
26. Eggenhuisen JT, McCaffrey WD (2012) The vertical turbulence structure of experimental turbidity currents encountering basal obstructions: implications for vertical suspended sediment distribution in non-equilibrium currents. *Sedimentology* 59(3):1101–1120. <https://doi.org/10.1111/j.1365-3091.2011.01297.x>
27. Jung JH, Yoon HS (2016) Effect of scour depth on flow around circular cylinder in gravity current. *Ocean Eng* 117:78–87. <https://doi.org/10.1016/j.oceaneng.2016.03.025>
28. Bhaganagar K (2017) Role of head of turbulent 3-D density currents in mixing during slumping regime. *Phys Fluids* 29(2):020703. <https://doi.org/10.1063/1.4974353>
29. La Rocca M, Adduce C, Sciortino G, Pinzon AB (2008) Experimental and numerical simulation of three-dimensional gravity currents on smooth and rough bottom. *Phys Fluids* 20(10):106603. <https://doi.org/10.1063/1.3002381>
30. Lombardi V, Adduce C, La Rocca M (2017) Unconfined lock-exchange gravity currents with variable lock width: laboratory experiments and shallow-water simulations. *J Hydraul Res*. <https://doi.org/10.1080/00221686.2017.1372817>
31. Baas JH, Van Kesteren W, Postma G (2004) Deposits of depletive high-density turbidity currents: a flume analogue of bed geometry, structure and texture. *Sedimentology* 51(5):1053–1088. <https://doi.org/10.1111/j.1365-3091.2004.00660.x>
32. Nogueira HIS, Adduce C, Alves E, Franca MJ (2013) Analysis of lock-exchange gravity currents over smooth and rough beds. *J Hydraul Res* 51(4):417–431. <https://doi.org/10.1080/00221686.2013.798363>
33. Cenedese C, Nokes R, Hyatt J (2016) Lock-exchange gravity currents over rough bottoms. *Environ Fluid Mech*. <https://doi.org/10.1007/s10652-016-9501-0>
34. Varjavand P, Ghomeshi M, Dalir AH, Farsadizadeh D, Gorgij AD (2015) Experimental observation of saline underflows and turbidity currents, flowing over rough beds. *Can J Civil Eng* 42(11):834–844. <https://doi.org/10.1139/cjce-2014-0537>
35. Alexander J, Morris SA (1994) Observations on experimental, nonchannelized, high-concentration turbidity currents and variations in deposits around obstacles. *J Sediment Res* 64(4a):899–909. <https://doi.org/10.1306/d4267f00-2b26-11d7-8648000102c1865d>
36. Morris SA, Alexander J (2003) Changes in flow direction at a point caused by obstacles during passage of a density current. *J Sediment Res* 73(4):621–629. <https://doi.org/10.1306/112502730621>
37. Choi S-U, Garcia MH (2001) Spreading of gravity plumes on an incline. *Coast Eng J* 43(4):221. <https://doi.org/10.1142/S0578563401000359>
38. Wilson RI, Friedrich H, Stevens C (2017) Image thresholding process for combining photometry with intrusive flow instruments. *J Hydraul Res*. <https://doi.org/10.1080/00221686.2017.1313320>
39. Adduce C, Sciortino G, Proietti S (2012) Gravity currents produced by lock exchanges: experiments and simulations with a two-layer shallow-water model with entrainment. *J Hydraul Eng* 138(2):111–121. [https://doi.org/10.1061/\(ASCE\)HY.1943-7900.0000484](https://doi.org/10.1061/(ASCE)HY.1943-7900.0000484)
40. Nogueira HIS, Adduce C, Alves E, Franca MJ (2014) Dynamics of the head of gravity currents. *Environ Fluid Mech* 14(2):519–540. <https://doi.org/10.1007/s10652-013-9315-2>
41. Ottolenghi L, Adduce C, Inghilesi R, Armenio V, Roman F (2016) Entrainment and mixing in unsteady gravity currents. *J Hydraul Res*. <https://doi.org/10.1080/00221686.2016.1174961>
42. Jacobson MR, Testik FY (2014) Turbulent entrainment into fluid mud gravity currents. *Environ Fluid Mech* 14(2):541–563. <https://doi.org/10.1007/s10652-014-9344-5>
43. Keevil GM, Peakall J, Best JL, Amos KJ (2006) Flow structure in sinuous submarine channels: velocity and turbulence structure of an experimental submarine channel. *Mar Geol* 229(3–4):241–257. <https://doi.org/10.1016/j.margeo.2006.03.010>

44. Wilson RI, Friedrich H, Stevens C (2015) Intrusive measurement evaluation for sediment-laden flows interacting with an obstacle. Paper presented at the 36th international IAHR world congress, The Hague, The Netherlands
45. Gray TE, Alexander J, Leeder MR (2005) Quantifying velocity and turbulence structure in depositing sustained turbidity currents across breaks in slope. *Sedimentology* 52(3):467–488. <https://doi.org/10.1111/j.1365-3091.2005.00705.x>
46. Ellison TH, Turner JS (1959) Turbulent entrainment in stratified flows. *J Fluid Mech* 6(03):423–448. <https://doi.org/10.1017/S0022112059000738>
47. Sequeiros OE, Spinewine B, Garcia MH, Beaubouef RT, Sun T, Parker G (2009) Experiments on wedge-shaped deep sea sedimentary deposits in minibasins and/or on channel levees emplaced by turbidity currents. Part I. Documentation of the flow. *J Sediment Res* 79(8):593–607. <https://doi.org/10.2110/jsr.2009.064>
48. Ermanyuk E, Gavrilov N (2005) Interaction of internal gravity current with an obstacle on the channel bottom. *J Appl Mech Tech Phys* 46(4):489–495. <https://doi.org/10.1007/s10808-005-0100-y>
49. Lane-Serff GF, Beal LM, Hadfield TD (1995) Gravity current flow over obstacles. *J Fluid Mech* 292:39–53. <https://doi.org/10.1017/S002211209500142X>
50. Rottman JW, Simpson JE, Hunt JCR, Britter RE (1985) Unsteady gravity current flows over obstacles: some observations and analysis related to the phase II trials. *J Hazard Mater* 11:325–340. [https://doi.org/10.1016/0304-3894\(85\)85044-5](https://doi.org/10.1016/0304-3894(85)85044-5)
51. Wilson RI, Friedrich H, Stevens C (2017) Turbulent entrainment in sediment-laden flows interacting with an obstacle. *Phys Fluids* 29(3):036603. <https://doi.org/10.1063/1.4979067>
52. Baas JH, Best JL (2002) Turbulence modulation in clay-rich sediment-laden flows and some implications for sediment deposition. *J Sediment Res* 72(3):336–340. <https://doi.org/10.1306/120601720336>
53. Kubo Y (2004) Experimental and numerical study of topographic effects on deposition from two-dimensional, particle-driven density currents. *Sediment Geol* 164(3–4):311–326. <https://doi.org/10.1016/j.sedgeo.2003.11.002>
54. Stagnaro M, Bolla Pittaluga M (2014) Velocity and concentration profiles of saline and turbidity currents flowing in a straight channel under quasi-uniform conditions. *Earth Surf Dyn* 2(1):167–180. <https://doi.org/10.5194/esurf-2-167-2014>